Enhancing detection of underground nuclear tests with unconventional tracers

Aliaksei Pazdniakou, Valeri V. Mourzenko, Jean-François Thovert, Pierre Adler, Eric Pili

ORCID numbers: Pierre M. Adler: 0000-0001-9952-9294 Eric Pili: 0000-0002-5328-2107

January 8, 2024

Enhancing detection of underground nuclear tests with unconventional tracers

Aliaksei Pazdniakou[1], Valeri Mourzenko[2], Jean-François Thovert[2], Pierre M. Adler[1], and Eric Pili[3]

[1]*Sorbonne Université, 4 place Jussieu, 75252 Paris Cedex 05*

[2]*Institut Pprime, CNRS, SP2MI, Futuroscope Chasseneuil and*

[3]*CEA, DAM, DIF, F-91297 Arpajon, France*

Abstract

Underground nuclear explosions (UNEs) generate important flows of air which carry tracers either initially present in the rock or soil or created by the explosion. These tracers can be observed not only at monitoring sites, but also at the test site. They could be used to enhance monitoring of radioxenon, widely used to detect UNEs, which can be impeded by several factors. We first developed a model for non-isothermal one-phase flow, heat and mass transfer, and tracer transport through fractured porous media. Taking as an example the conditions of the North-Korean site at Punggye-ri, we provide estimations for the emission of water vapor and CO_2 at the test site, and for the emission of radon and xenon at the test site and at the Takasaki monitoring site in Japan. The influence of the geological conditions is investigated. It is shown feasible to enhance detection of radioxenon related to an underground nuclear explosion at a given monitoring station by detecting, a short time beforehand at the test site, the concomitant emission of water vapor by satellite imaging, providing low to moderate wind conditions. If only contributed from the soil, CO_2 scavenged by the gas emitted following an UNE cannot be detected from satellite imaging. Although contributed from the rocks, including the vaporized cavity, radon cannot be detected at the monitoring site. For its own sake as for comparison, radioxenon is also examined in the same conditions as the studied tracers at the test site and at the monitoring site.

I. INTRODUCTION

Underground nuclear explosions (UNEs) induce important changes in the host rock with creation of a cavity, a chimney and fractures, as well as strong flows of air and water vapor. The nuclear nature of an underground explosion can only be ascertained if some radionuclides associated with the detonation are emitted to the atmosphere. Thus, radionuclide detection by monitoring stations is one of the cornerstones in the International Monitoring System (IMS) of the Comprehensive nuclear Test-Ban Treaty (CTBT), especially thanks to the monitoring of radioxenon activities (Kalinowski and Schulze, 2002; Kalinowski et al., 2010). However, detection of radionuclides emitted from underground nuclear tests can be impeded by several factors : (i) the potentially low level of radioactivity emitted at the test site, especially for low-yield nuclear testing, due to containment practices (e.g., Carothers et al., 1995) and the natural effects of the geosphere to limit emissions to the atmosphere (e.g., Pazdniakou et al., 2022); (ii) long distances from the potential nuclear test sites to the limited number of monitoring stations, going with radioactive decay as well as strong dilution along atmospheric transport (e.g., Eslinger et al., 2015) ; (iii) addition of the same radionuclides emitted from civilian activities (e.g., Achim et al., 2016). Therefore, there is a need to strengthen detection of radionuclides related to an underground nuclear explosion.

This work investigates gaseous species other than the usual radionuclides of interest that could be emitted to the atmosphere following a nuclear test, then used as a trigger signal to enhance detection of the radionuclides. These tracer emissions could possibly be detected either at the monitoring stations or, thanks to remote sensing, directly at their emission point. The objective of this work is to analyze the transport up to the ground surface, when the host rock has reached a stable state, of tracers either initially present in the medium, such as radon (located everywhere in the rock matrix) or carbon dioxide (located only in the soil layer), or generated in the nuclear cavity, such as water vapor. The outputs of these tracers are compared with those obtained in the same conditions for radioxenon, also generated in the cavity.

Radioxenon will be considered both at the nuclear test site, supposed to be the North-Korean Punggye-ri site, and at a monitoring site, supposed to be the IMS RN38 monitoring station located in Tagasaki, Japan (e.g., Goodwin et al., 2021). This hypothesis is made for the sake of realism and for the estimation of the dilution factor due to atmospheric transport

(see further below). We also supposed that the studied underground nuclear explosion occurred in granitic rocks (Coblentz and Pabian, 2015). Radon will also be considered both at the nuclear site and at the monitoring site, in order to compute its potential contribution. Carbon dioxide and water vapor will only be considered for their emissions at the nuclear test site, as the atmospheric mass budget of these gas species is far too high along the transport from the test site to the monitoring station to be affected by these emissions. However, our choice of water vapor and carbon dioxide is guided by their common monitoring from remote sensing techniques (e.g., Bovensmann et al., 2010; Wulfmeyer et al., 2015).

The analysis of tracers transferred to the atmosphere after an underground nuclear test regained interest since the CTBT opened for signature in 1996. The relevant literature, here limited to analog experiments conducted at former nuclear test sites and related modeling, can be summarized as follows. An early experiment by Carrigan et al. (1996) simulated a 1 kiloton explosion produced by chemical explosives at a depth of 400 m at the Nevada National Security Site (NNSS, USA), with two tracers, ^{3}He and SF_6, having sufficiently distinctive diffusivities to be observed at the ground surface with a contrasted delay, evidencing barometric pumping. The chimney resulting from the shaft-type Barnwell test conducted in 1989 at the NNSS was used repeatedly as a testbed for injections of various tracers in various conditions, variably explained with modeling (Carrigan et al., 2016, 2022; Olsen et al., 2016; Bourret et al., 2018; Johnson et al., 2019). Also at the NNSS, Carrigan et al. (2020) reported a gas tracer experiment from the chimney of the tunnel-type 1989 Disko Elm test conducted in well-contained conditions with a gas permeability much lower than the Barnwell testbed; they noticed that gases detected at the surface resulted from fractures of extremely small aperture and that leakage also occurred directly from the tunnel portal, the tunnel wall being at a shorter distance from the chimney than the ground surface.

Several papers were devoted to radon. At the NNSS, Wollenberg et al. (1977) examined the relations between UNEs and radon emanation, but they observed no systematic correlation except due to ground shaking in alluvium. Burnett et al. (2021) revisited this topic taking benefit of lower yield chemical explosions (1–50 t), but again no clear-cut conclusion could be drawn from these experiments. During pressurization of the Barnwell chimney, Carrigan et al. (2016) observed anomalously high radon activities suggesting that radon levels may be a signal for gas transport following a suspected UNE.

Regarding the modeling of gas transport associated with UNEs, with a few exceptions

such as in Sun and Carrigan (2012, 2016), Carrigan et al. (2016, 2019, 2022) and Pazdniakou et al. (2022), the thermal effects are neglected and only the long-term evolution is analyzed, when barometric pumping is predominant. A few papers used a simplified approach based on Nilson et al. (1991) with a single vertical fracture or a series of such fractures periodically arranged (Lowrey et al., 2013, 2015; Harp et al., 2019, 2020). Most studies used the more general though still simplified dual permeability approach of Barenblatt et al. (1960) with various degrees of sophistication and various softwares. Sun and Carrigan (2012, 2016) and Harp et al. (2018) used two-phase flow while Carrigan et al. (1996), Sun and Carrigan (2012), Lowrey et al. (2013, 2015), Sun et al. (2014), Jordan et al. (2014, 2015) and Bourret et al. (2018, 2020) used single phase flow. Among the two-phase flow simulations, some considered water as immobile in the pore space; only gases could partition into the aqueous phase. Recently, Sun et al. (2022) included some more realistic features such as cavity partitioning processes combined with seepage to the host rock and venting to ground surface of the cavity gases, with simplified descriptions. Pazdniakou et al. (2022) went one step further in taking reality into account, modeling two-phase flow with emphasis on phase change, heat transfer and tracer transport through fractured porous media built from a precise description of a realistic fracture network hosted in a rock matrix.

The present work proposes to study the transport of underground tracers up to the atmosphere after an UNE by a detailed numerical analysis of the phenomena. Because of the high pressures and temperatures generated by the explosion, a realistic modeling should include the fluid compressibility and the temperature variations in addition to standard fluid flow and tracer transport, including barometric pumping. Moreover, the domain is heterogeneous with porosity variations and fractures which were partly induced by the explosion itself. The exact geometry and properties of the fracture network are taken into account which significantly increases the computation cost, but enables a more precise quantification of the phenomena. Related studies with the same methodology were conducted by Mourzenko et al. (2014) for barometric pumping and by Pazdniakou et al. (2022) for two-phase flow with emphasis on phase change, heat transfer and tracer transport.

This paper is organized as follows. Section II describes the basic configurations to be used in this paper and the major petrophysical quantities. Then, Section III provides the basic flow, energy and tracer equations which govern the phenomena. Their discretization and resolution are only briefly sketched. Among the considered tracers, water vapor and

carbon dioxide are of interest only at the test site, while radioxenon and possibly radon are of interest at the monitoring sites. The two first ones are addressed in Section IV and the second ones in Section V. A few concluding remarks are given in Section VI.

II. THE CONFIGURATION AND ITS BASIC PETROPHYSICAL PROPERTIES

Details on the phenomenology of underground nuclear explosions are beyond the scope of this work and can be found in Johnson et al. (1959), Boardman et al. (1964), Carothers et al. (1995) and Derlich (1970). As an example, we will consider throughout this paper a 150 kt-explosion at a depth of 630 meters in a granitic rock (saturated with water at this depth) that would produce according to Boardman et al. (1964) a cavity with a radius of ca. 50 meters and develop a chimney with an height of ca. 220 m filled with rubbles. The overburden above the chimney would thus be ca. 400 m thick. In order to preserve the volume of the cavity, this spherical concept is recast into a slightly different parallelipipedic model, as follows.

The situation can be roughly schematized as in Fig.1, which is the same as in Pazdniakou et al. (2022). The cavity created by the explosion is rapidly topped by a chimney and lined at the bottom with some magma; the union of these three regions is called in this paper the damaged zone. This zone is embedded in a fractured porous medium; some of these fractures may be present before the nuclear test, but many of them are created by the explosion itself.

At the final stage displayed in Fig.1, a fracture network is assumed to reach the ground surface, thus creating a percolating fractured porous medium located over the chimney, which provides a path for the hot pressurized gas emitted to the atmosphere before any detection. This network is not included in what is called the damaged zone. The numerical code which will be described in the next section allows us to simultaneously simulate the fractured porous medium located above the damaged zone, the damaged zone and the intact porous medium embedding both of them as schematically displayed in Fig.1. The complete simulation domain is a parallelipipedon of size $200 \times 200 \times 650$ m^3. The permeability of the porous matrix is $K_m = 10^{-16}$ m^2, and its porosity is $\varepsilon = 0.01$ or 0.05; the first value mimics the properties of a granitic rock while the second one is used to explore the influence of the porosity.

The damaged zone located inside the porous medium is also parallelipipedic and measures

$100 \times 100 \times 200$ m^3. Here, it is modeled as a uniform porous medium with much higher permeability $K_m = 8.33\,10^{-8}$ m^2 and porosity $\varepsilon = 0.29$.

The fracture network inside the domain (see Fig.1b) consists of $N_f = 192$ or 384 regular hexagonal fractures of radius 20 m. The centers of the fractures are randomly generated inside the $100 \times 100 \times 400$ m^3 domain located over the chimney. The fracture network percolates along the z-axis, i.e., it continuously connects the chimney and the ground surface. The same aperture $b = 10^{-3}$ m is assigned to all the fractures; the corresponding transmissivity is $\sigma_f = 8.33\,10^{-11}$ m^3.

All the computations are initiated assuming normal physical conditions inside the domain outside of the damaged zone. The normal physical conditions correspond to the temperature $T_0 = 288.15$ K, the gas pressure $p_0 = 101330$ Pa, and the gas density $\rho_0 = 1.2172$ kg/m^3.

Dirichlet boundary conditions corresponding to the normal state are applied at all the sides of the simulation domain. At the ground surface, the Dirichlet boundary conditions are given by

$$T(z = 650) = 288.15\,\mathrm{K}\ ,\ C_t(z = 650) = 0\ ,\ p(z = 650) = p_0 + A_p \sin(\omega_p t)\ \mathrm{Pa} \qquad (1)$$

where the amplitude A_p is 10^3 Pa, and the frequency $\omega_p = 10^{-5}$ Rad/s which corresponds to a period of 7.27 days.

The initial temperature inside the chimney is always equal to T_i=802.15 K while three initial pressures are investigated

$$P_0 = \ 50,\ 100,\ 200\ \mathrm{bars} \qquad (2)$$

The pressure condition $P_0 = 50$ bars corresponds to a cavity pressurized only by vaporization of its contained water, while $P_0 = 100$ and 200 bars could be viewed as resulting from additional gas sources, such as hydrogene, carbon dioxide, carbon monoxide or methane, due to different physico-chemical conditions.

Air is assumed to be a perfect gas and its density is given by

$$\rho = \rho_0 \frac{T_0}{T} \frac{p_0}{p} \qquad (3)$$

III. GOVERNING EQUATIONS AND NUMERICAL RESOLUTION

The main objective of this paper is to analyze the transport and the resulting surface emission of tracers present in the medium or created by the explosion due to the initial

pressure and temperature after the test. In order to meet this objective, a single phase code was developed which solves the relevant flow, energy and tranport equations which are now described. The physical properties are essentially the same as in Table I of Pazdniakou et al. (2022).

A. Air flow

In order to incorporate thermal effects and obtain a more general model, a fully compressible formulation is adopted here, at the expense of some computational overhead. This is also necessary, considering the physical conditions ($p \approx 2\,10^7$ Pa, $T \approx 10^3$ K) typical for the applications of interest.

Thus, the air flow inside the porous matrix of permeability K_m and porosity ε_m is described by mass conservation and Darcy equations

$$\frac{\partial(\varepsilon_m \rho_g)}{\partial t} + \nabla \cdot (\rho_g \mathbf{v}) = 0 \tag{4a}$$

$$\mathbf{v} = -\frac{K_m}{\mu_g}(\nabla p - \rho_g \mathbf{g}) \tag{4b}$$

where ρ_g is the gas density, t the time, μ_g the gas viscosity, $\mathbf{v}$ the Darcy seepage velocity, p the gas pressure, and $\mathbf{g}$ the gravitational acceleration.

Similar equations can be written for air flow in fractures

$$\frac{\partial(b\rho_g)}{\partial t} + \nabla_S \cdot (\rho_g \mathbf{q}) + [\rho_g \mathbf{v}] \cdot \mathbf{n} = 0 \tag{5a}$$

$$\mathbf{q} = -\frac{\sigma_f}{\mu_g}\{\nabla_S p - \rho_g \mathbf{g}(\mathbf{I} - \mathbf{nn})\} \tag{5b}$$

where b denotes the fracture aperture, ∇_S the two-dimensional gradient operator in the fracture plane, $\mathbf{q}$ the in-plane flow rate per unit width, $\mathbf{n}$ the unit normal vector to the fracture, $[\rho_g \mathbf{v}]$ the difference in $\rho_g \mathbf{v}$ value evaluated at the $+\mathbf{n}$ and $-\mathbf{n}$ sides of the fracture, and $\mathbf{I}$ the unit tensor. The fracture porosity is supposed to be equal to 1. Flow continuity at the fracture/matrix interfaces is ensured by the exchange term. The fracture transmissivity is obtained by assuming Poiseuille law for the rectangular channel

$$\sigma_f = \frac{b^3}{12} \tag{6}$$

The gas pressure is related to the gas density by using the ideal gas law

$$p = \rho_g \frac{R_g}{M_g} T_g \tag{7}$$

where $R_g = 8.3145\ \mathrm{J\,K^{-1}\,mol^{-1}}$ is the ideal gas constant, M_g the gas molar mass ($M_g = 0.02896\ \mathrm{kg\,mol^{-1}}$ for the air), and T_g the gas temperature.

B. Energy conservation

The geometry of the medium is constant and unchanged by the transport processes. The heat transport is incorporated into the model since it may influence both gas flow and tracer transport. Two modes of heat transport are included, namely conduction and convection. Radiative transport is always ignored.

The hypothesis of local thermal equilibrium is adopted which assumes a single temperature T for the solid and the gas phases

$$T = T_s = T_g \tag{8}$$

The energy conservation for the porous matrix can be written as

$$\frac{\partial(\varepsilon_m \rho_g c_g T + (1-\varepsilon_m)\rho_s c_s T)}{\partial t} + \nabla \cdot (\mathbf{v}\rho_g c_g T - \lambda_m \nabla T) - \varepsilon_m \frac{\partial p}{\partial t} = 0 \tag{9}$$

where c_g and c_s are the gas and the solid phase specific heat capacities; ρ_s is the solid phase density, and λ_m the effective heat conductivity of the porous matrix, which is approximated by

$$\lambda_m = \varepsilon_m \lambda_g + (1-\varepsilon_m)\lambda_s \tag{10}$$

where λ_g and λ_s are the gas and the solid phase conductivities (Nield and Bejan, 2006). The last term in (9) is a combination of the pressure work and of the viscous dissipation; for sake of brevity, it will be simply called compression work in the following.

Similarly, the energy equation for the fractures is given by

$$\frac{\partial(b\rho_g c_g T)}{\partial t} + \nabla_S \cdot (\mathbf{q}\rho_g c_g T - \Lambda_f \nabla_S T) + [\mathbf{v}\rho_g c_g T - \lambda_m \nabla T] \cdot \mathbf{n} - b\frac{\partial p}{\partial t} = 0 \tag{11}$$

where Λ_f is the fracture thermal transmissivity, which is approximated for a plane channel by

$$\Lambda_f = b\lambda_g \tag{12}$$

The continuity of the heat flux at the fracture/porous matrix interface is accounted through the exchange term $[\mathbf{v}\rho_g c_g T - \lambda_m \nabla T] \cdot \mathbf{n}$ which is evaluated in the same way as the similar term for the air flow.

C. Tracer transport

The tracer is supposed to be chemically inert. It does not react with the material of the porous matrix and does not undergo any changes during transport, except radioactive decay for ^{133}Xe and ^{222}Rn (see further below).

The tracer transport inside the porous matrix is described by the convection-diffusion equation as

$$\frac{\partial(\varepsilon_m \rho_g C_t)}{\partial t} + \nabla \cdot (\mathbf{v} \rho_g C_t) - \nabla \cdot \left(D \overline{D} \rho_g \nabla C_t \right) = W \tag{13}$$

where C_t is the tracer mass fraction, D the molecular diffusion coefficient of the tracer, and $\overline{D}$ the effective diffusivity of the porous matrix which can be approximated by Archie's law (see Adler, 1992) as

$$\overline{D} = \varepsilon_m^{1.4} \tag{14}$$

W (kg m^{-2}s^{-1}) is a source (or well) term which represents the generated mass of tracer per unit volume of porous medium in an algebraic sense. For instance for radon, it corresponds to the sum of the generated mass and of the radioactive decay.

An analogous equation describes the tracer transport inside the fractures

$$\frac{\partial(b \rho_g C_t)}{\partial t} + \nabla_S \cdot (\mathbf{q} \rho_g C_t) - \nabla_S \cdot (D \Sigma_f \rho_g \nabla_S C_t) + [\mathbf{v} \rho_g C_t - D \overline{D} \rho_g \nabla C_t] \cdot \mathbf{n} = W_f \tag{15}$$

where the last term in the left hand side describes the exchange between the porous matrix and the fractures; the generated mass is neglected in the fractures since the corresponding volume is very small; Σ_f is the fracture diffusional conductivity, which is given for a plane channel by Adler et al. (2012)

$$\Sigma_f = b \tag{16}$$

As for the aforementioned transport equations, the tracer flux continuity at the fracture/porous matrix interface is ensured through the exchange term. Finally, W_f is the analogous of W for fractures.

D. Numerical

Briefly speaking, the simulation domain is discretized, namely the fractures by triangles, and the porous matrix by tetrahedra. The size of the meshing elements does not exceed a prescribed limit δ. The generated fracture network is meshed with triangles and inserted

inside the porous matrix according to the procedure detailed by Koudina et al. (1998) and Huseby et al. (1997). Based on this initial mesh, the rest of the space is meshed with tetrahedra (Adler et al, 2012).

Then, all the transport equations constituting the model are discretized following the finite volume methodology. The variables of interest such as pressure, temperature, and concentration are defined at the mesh nodes, i.e., the vertices of tetrahedra and triangles. Inside the porous matrix, the control volumes are formed around the nodes by taking one fourth of each tetrahedron incident to the node. In the presence of fractures, the fracture element and the two adjacent porous matrix elements are considered separately in the triple control volume technique (3CV); three unknowns are defined for the three conservation equations over those elements.

The discretized equations are solved by the conjugate gradient method suitably adjusted to each one of them.

The flow equations are solved for a given temperature by a Picard scheme associated to the conjugate gradient method since compressibility generates non linearities. Then, the energy equations are solved for a given pressure field and their solution is injected back into the flow equations. This loop is repeated until prescribed overall tolerances are verified for p and T.

Then, the linear and independent discretized tracer transport equations are solved by the conjugate gradient method. In order to limit numerical dispersion, the convection-diffusion equations are discretized with a flux limiting scheme which employs a SuperBee function (Harten, 1993; Sweby, 1984) generalized to three dimensions. Also, a particular attention is paid to the exchange between the fractures and the porous matrix.

The reader is referred to the Appendix 2 of Pazdniakou et al. (2022) for further details.

IV. OUTPUTS AT THE NUCLEAR TEST SITE

A. General

As detailed in Section II, four petrophysical conditions were studied, namely the matrix porosity ϵ= 0.01 and 0.05, and the number of fractures N_f=192 and 384. In addition, three initial pressures in the cavity were used, namely P_0= 50, 100 and 200 bars. Generally

speaking, calculations were made for all the parameters even if only few results were selected for presentation in the following.

It might be useful to give a short overview of the influence of these three parameters on the simplest quantity, namely the total mass flow of gas $M_g(t)$ at the ground level.

Full results for $M_g(t)$ are given in Fig.2 where it is seen that the masses of gas which are emitted after a test are enormous, of the order of 1000 to 10000 tons. Other calculations in analogous petrophysical conditions showed that most of these masses are emitted by the few fractures which intersect the ground surface. Moreover, the influence of the atmospheric pressure fluctuations (1) on $M_g(t)$ are not clearly visible for the first 15 days.

A paradoxical feature is that, at a given time, $M_g(t)$ appears to be a decreasing function of the matrix porosity ϵ. This can be understood if one makes clear that the permeability of the porous medium is unchanged and always equal to 10^{-16} m^2; hence, it is only the storativity of the medium which one sees at work in this comparison. In a sense, the outflow of gas is delayed when ϵ is increased without changing the permeability.

For a given value of ϵ, $M_g(t)$ is an increasing function of N_f as expected.

Finally, $M_g(t)$ is an increasing function of the initial pressure P_0 in the cavity as it should. However, the relation is not linear.

B. Water vapor

We consider that the initial mass of water contained in the nuclear cavity is about 5000 tons. This corresponds to the quantity of water contained in sphere of porous rock with a radius of 50 m and a porosity of 0.01, before its vaporization. Considering the total mass of air contained in the damaged zone and air density at the considered pressures, the mass fraction of water vapor is given by $C = 22.3/P_0$, hence respectively 0.446, 0.223 and 0.112 for 50, 100 and 200 bars. This represents the lower boundary of the range of water content in the system. The upper boundary is given by considering a mass fraction equal to 1.

1. Surface emission of water vapor

The mass flow rate Q_{H_20} and the total mass M_{H_20} transferred to the atmosphere are displayed in Fig.3. Q_{H_20} has a complex behaviour which is detailed in (a) and (b). It

starts increasing after some delay which corresponds to the influence of the porous matrix; the delay decreases with P_0. Then, after a few minutes as shown by (b), Q_{H_20} decreases; the time for which Q_{H_20} is maximal decreases with P_0. Then, the decrease is not exactly exponential and one can see a slight influence of the fluctuations of the atmospheric pressure (1).

The mass flow rate in (b) is an increasing function of time which smooths out the complex behaviour of Q_{H_20}. Only the first few hours are represented.

2. Detectability at the nuclear test site

A key question is wether or not this sudden water addition in the atmosphere at the nuclear test site could be detected using satellite imaging. This would be a signal that radioxenon is emitted to the atmosphere, indicating that a particular attention should be devoted to collection and analysis of air samples in the emitted plume whose position can be simulated by atmospheric transport modeling (e.g., Maurer et al., 2018). A first approach is to compare the released mass of water vapor to the water already present in the atmosphere. As shown in Fig.3c, the mass of water vapor released in 12 hours ranges from ca. 10 to 60 tons depending on the initial cavity pressure and for the lower water content of the system (mass fraction ranging from 0.446 to 0.112), while it ranges from ca. 25 to 500 tons for the upper water content of the system (mass fraction of 1). A typical order of magnitude for the atmospheric water vapor concentration is 15.5 g/m^3 (McClatchey et al., 1972; Schlaepfer, 1998), which corresponds to about 600 tons for a 1000 m-high column located on the 200×200 m^2 surface area of the release. Hence, the water vapor added to the atmosphere in 12 hours represents from 2-10 % to 4-80% of the mass of water vapor in a column of atmosphere. These encouraging results require a more quantitative analysis.

The monitoring of gas emissions from remote sensing techniques usually considers the integrated amount of the gas species along a vertical column of atmosphere. For water vapor, this quantity varies according to the climate zones and seasons (see Appendix, Table I) from ca. 4 kg/m^2 in winter for the subartic zone (the driest conditions) to ca. 42 kg/m^2 for the most humid conditions at the tropical zone (McClatchey et al, 1972; Schlapfer, 1998). At midlatitudes, the integrated amount of water vapor ranges from ca. 9 kg/m^2 in winter to ca. 30 kg/m^2 in summer. Classically, the variation of the water vapor content in the atmosphere

that can be detected by satellite imaging is about 5% (Gao and Kaufman, 2003). A lower boundary is about 2% (Mao et al., 2010; He and Liu, 2021; Rodolphe Marion, pers. comm.), which corresponds to a variation of the water content ranging from 0.08 kg/m^2 in Winter for the subartic zone to ca. 0.84 kg/m^2 for the tropical zone (from 0.05 kg/m^2 in Winter to 0.6 kg/m^2 in Summer at midlatitudes). Details are given in the Appendix, Table I.

Let us now estimate if the plume of water vapor flux emitted at the nuclear test site can be detected, which means it is likely to generate such variations of the atmopsheric water content, considering its dispersion by wind over some distance before its quantification by satellite imaging. This is classically done by a Gaussian plume inversion method, as described for instance in Bovensmann et al. (2010) and Varon et al. (2018), which is here used to get a first appraisal of the detectability. Details are given in the Appendix. It comes that even for the less favorable conditions (initial cavity pressure of 50 bars and low water content), the water plume emitted with a mass flow rate of ca. 0.25 kg/s in the first 3 hours could be detected in low wind conditions (wind speed of 0.1 m/s) whatever the climate zones and seasons, except the tropical zone where the natural water content of the atmosphere is too high. In particular, at the midlatitudes relevant for the Punggye-ri test site, detection is feasible whatever the season providing low wind conditions. For initial cavity pressures of 100 or 200 bars, still with low initial water content, detection is feasible at wind speed up to 1 m/s in the subartic regions (Winter and Summer) and at midlatitudes in Winter, while detection is feasible whatever the climate zones and seasons for low wind conditions. For the high water vapor content (mass fraction of 1 in the damaged zone), corresponding to initially saturated conditions, detection is feasible whatever the climate zones and seasons for wind speed up to 1 m/s, while detection is feasible even at wind speed of 10 m/s in cold regions or seasons. Detection would be feasible in high wind conditions (20 m/s) only in Winter (subartic and midlatitude zones). On average, detection occurs in 70% of the considered cases for a detectability of 2% of the variation of the water vapor content, while detection occurs in 57% of the considered cases for a detectability of 5% of the variation of the water vapor content (see Appendix, Tables III and IV).

3. Influence of the petrophysical properties

The influence of the petrophysical properties of the surrounding medium on the mass flow rates was studied. Two porosities ($\epsilon = 0.01$ and 0.05) and two fracture numbers (N_f= 192 and 384) were investigated and the results are seen in Fig.4 for an initial cavity pressure P_0 equal to 100 bars. When the porosity increases, the mass flow rate and the total mass of water transferred to the atmosphere decrease moderately. When the number of fractures increases, the mass flow rate and the total mass of water transferred to the atmosphere increase strongly. The geological conditions are thus important factors controlling the emission of gas to the atmosphere.

The inclusion of fractures in the porous medium is computationnaly very expensive and one may wish to compare the results of the full model to the results obtained with an homogeneous porous medium. The permeability of the equivalent medium is calculated for the fractured zone by a time independent code (see for instance Bogdanov et al., 2003); it is found equal to $6.48\,10^{-13}$ m^2 for N_f=192. Calculations were performed for a configuration where the fractured porous medium (in grey in Fig.1a) is replaced by this equivalent porous medium. The outputs for the homogeneous case are compared with the ones for the fractured porous medium in Fig.5; they show two contrasted time evolutions, but the orders of magnitude of the mass flow rates and total mass of water vaport transferred to the atmosphere are the same. This emphasizes that there is still a need to carefully consider fracture networks for detailed computations, but that rapid estimates obtained from simplified configurations remain relevant. Three periods can be observed in the evolution of the outputs. Q_{H_20} and M_{H_20} do not start increasing immediately; there is a delay during which the gas first fills in the porosity. Then, the mass flow rate starts increasing quickly before it decreases slowly.

C. Carbon dioxide

Carbon dioxide is supposed to be sourced by the biological activity in the soil. We assume a layer of soil of height h at the top of the medium without any fracture. The permeability of the soil is assumed to be 10^{-12} m^2 and its porosity is equal to 0.3. The macroscopic

diffusion coefficient is determined by using Archie's law (14) with D=1.6 10^{-5} m^2/s

$$D\overline{D} = 2.97\,10^{-5}\ \mathrm{m}^2 \tag{17}$$

A typical value of the mass flow rate of carbon dioxide m_{CO_2} at the ground surface is 300 mg m^{-2} hour^{-1} (Risk et al, 2002).

Here, the initial mass fraction c_0 and the generated mass per unit volume of porous medium W_{CO_2} (cf (13)) are necessary in order to determine the evolution of the amount of carbon dioxide underground and at the ground surface. In order to estimate these values, a simple one-dimensional model is used. In a steady state, the boundary conditions at the ends of the layer are the following. The concentration is assumed to be 0 at the ground surface (at the first order, the atmospheric CO_2 concentration of ca. 400 ppm is negligible when compared to the soil concentration), and the flux is 0 at the bottom of the soil layer. One readily obtains

kg/m-3s-1

$$W_{CO_2} = \frac{m_{CO_2}}{h} = 8.33\,10^{-9}\ \mathrm{kg\ m^{-2}s^{-1}}\ , \quad c_0 = \frac{W}{\rho_g D}\frac{h^2}{3} = 7.6\,10^{-2} \tag{18}$$

This generation is numerically implemented as follows. The fracture triangles whose gravity centers are closer than h to the ground surface are removed from the fracture list; the porous matrix tetrahedra whose gravity centers are closer than h to the ground surface are given an initial mass fraction equal to c_0 and a generated mass equal to W_{CO_2}. The bottom of the soil layer is not smooth because of this implementation and the total volume where CO_2 is generated corresponds to a layer of equivalent thickness approximately equal to 6 m. Therefore, the expected numerical mass flow rate m'_{CO_2} at the ground surface is 0.6×300 = 180 mg m^{-2} hour^{-1}, i.e. 173 kg/day.

?

units?

Results are given in Fig.6. Fig.6a shows the mass flow rates of CO_2 transferred to the atmosphere as a function of time for the usual three values of the initial cavity pressures. One can see that after the sudden increase of $M_c(t)$ due to the arrival of the gas from the cavity which wipes out the carbon dioxide present in the soil, the curves are more or less linear and parallel. This stationary regime indicates that the CO_2 produced in the soil layer is evacuated to the atmosphere.

Fig.6b shows the total mass of CO_2 transferred to the atmosphere. The slight undulations are due to the atmospheric fluctuations (1). The average slope, estimated for P_0=100 bars by taking two values separated by one day, is equal to 189 kg/day, in agreement with the input m'_{CO_2}.

Fig.6c shows a planar view of the mass flow rate of CO_2 emitted at the ground surface after t=12.9 days, where one can observe a distinctive circular shape. Recall that the fractures stop approximately 6 m below this surface and that neither their intersection with the horizontal plane nor the distribution of the gas fluxes form any particular shape.

Determining if this circular structure is a general feature of gas flow through any fracture network topped with a porous layer is beyond the scope of this study. If so, searching for this distinctive feature could be an additional signal of gas emission to the atmosphere.

The detectability of CO_2 emitted at the ground surface by remote sensing techniques can be assessed in the same manner as for water vapor. However, the orders of magnitude of the reservoir and flux are much less favorable for CO_2 than for H_2O. With an average mass fraction of CO_2 in the atmosphere of 410 ppm, the CO_2 mass contained above the 200×200 m^2 field in a column of 1000 m is about 32 tons, while the emission is ca. 180 kg per day, hence ca. 0.5%. The integrated CO_2 content in the atmosphere is of the order of 6 kg/m^2 (total atmospheric CO_2 mass according to Pellegrini et al. (2022) divided by the total surface area of the Earth). Unlike water vapor, this value is not subjected to strong variations with climate zones or seasons, but will show diurnal cycles due to respiration modulated by daylight photosynthesis. Assuming that satellite imaging is able to detect a variation of 5% of this CO_2 content and using the same Gaussian plume inversion method as for water vapor, it comes that very few conditions can lead to a detection of CO_2 emissions at the ground surface of a nuclear test site following an UNE, with satellite imaging. Only the very high initial cavity pressure of 200 bars would lead to a detection, providing low wind speed (0.1 m/s).

V. OUTPUTS AT THE NUCLEAR SITE AND AT THE MONITORING SITE

In addition to the detection of gas emissions at the test site, detection of tracers related to an UNE at the monitoring site could possibly help to identify the arrival of radioxenon. Atmospheric transport from the test site to the monitoring site goes with delay and dilution, should a given monitoring site be connected with the test site, depending on the meteorological conditions. In practice, dilution is expressed with a factor allowing to convert the emission expressed in Bq/s at the test site (here the Punggye-ri site in North Korea) into a volumetric activity concentration expressed in Bq/m^3 at the monitoring station (here the

IMS RN38 station at Takasaki, Japan). Goodwin et al. (2021) mentioned a dilution factor of 10^{-15} s/m^3, recalling it is known to vary by several orders of magnitude. A dilution factor $\eta = 7\,10^{-18}$ s m^{-3} is used here, in agreement with the range from 10^{-14} to 10^{-18} s/m^3 calculated by Sylvia Generoso (pers. comm., June 2023) using the Flexpart code (Stohl et al., 1998) with real meteorological data at 1 hour time-step for the entire year 2022 and for the same geographical conditions. The delay considered here is 1 day.

A. Radon

Among the naturally occuring tracers, radon is interesting as it shares similarities with radioxenon, being a heavy noble gas, highly diluted and measured through its radioactivity. Only ^{222}Rn is considered here; ^{220}Rn is neglected due to its much shorter half-life, but could be computed in the same way. Radon may have two origins; it is constantly generated everywhere in the porous medium and it is originally contained in the rock which is vaporized during the explosion. While the first source of radon is controlled by its emanation from the grain boundaries in the porous medium, the second source is controlled by the radium content of the vaporized rock. The physical constants of radon are the following. The atomic mass M_{Rn} is equal to 0.222 kg/mol. The molecular diffusion coefficient D is $1.05\,10^{-5}$ m^2/s. The radioactive decay constant λ_{Rn} is $2.1\,10^{-6}$ s^{-1}.

The radon activity W per unit volume of the porous medium, as used in (13), is the sum of two terms

$$W_{Rn} = \rho_s(1-\epsilon_m)EC_{Ra} - \lambda_{Rn}\rho_g\epsilon_m C_t \frac{N_{Av}}{M_{Rn}} \tag{19}$$

The first term corresponds to the ^{222}Rn emanated from the grains after decay from ^{226}Ra and the second one to its desintegration. C_t is the radon mass fraction (expressed in kg of radon per kg of air), as in (13). ρ_s is the solid density equal to 2690 kg/m^3 and N_{Av} is the Avogadro number. E is the emanation coefficient whose order of magnitude is 0.2 (Richon et al., 2005). C_{Ra} is the radium activity which is of the order of 55 Bq per kg of rock according to the same author.

At equilibrium W_{Rn}=0 and one can derive the mass fraction of radon in the porous medium when $\epsilon_m = 0.01$ and the local pressure is equal to p_a

$$C_t = \frac{\rho_s}{\rho_g}\frac{(1-\epsilon_m)}{\epsilon_m}\frac{EC_{Ra}}{\lambda_{Rn}}\frac{M_{Rn}}{N_{Av}} = 4.2\,10^{-13} \tag{20}$$

Another initial source of radon corresponds to the quantity present in the rock before the formation of the damaged zone (cavity and chimney), including the radon initially contained in the rock grains which are vaporized during the explosion and the quantity present in the porosity of this volume of rock. Since the radon initially contained in the rock grains is in equilibrium with the radium, the activities of radium and radon are equal. Therefore, the quantity Q_{Cav} of radon can be expressed in kg as

$$Q_{Cav} = \frac{(\rho_s(1-\epsilon_m)C_{Ra} + \epsilon_m C_{Rn})V_{Cav}}{\lambda_{Rn}} \frac{M_{Rn}}{N_{Av}} = 8\,10^{-8} \tag{21}$$

where V_{Cav} is the volume of the cavity ($0.5\,10^6$ m^3) and C_{Rn} is fixed to $8\,10^7$ Bq/m^3, an upper limit of the observed radon activities in the porosity of granitic rocks (Guillon, 2013). Similarly, the quantity Q_{Chim} of radon (expressed in kg) generated in the porosity of the rock volume before it becomes the chimney is

$$Q_{Chim} = \frac{\epsilon_m C_{Rn} V_{Chim}}{\lambda_{Rn}} \frac{M_{Rn}}{N_{Av}} = 19\,10^{-8} \tag{22}$$

where V_{Chim} is the volume of the chimney ($1.5\,10^6$ m^3). Therefore, $27\,10^{-8}$ kg of radon are present in the damaged zone at the beginning. The mass fraction in the damaged zone of porosity 0.3 and volume $2\,10^6$ m^3 is pressurized to the initial pressure P_0.

The ^{222}Rn surface flow rate at the test site and the volumetric activity concentrations at the monitoring site are shown in Fig.7. At the test site, the ^{222}Rn flow rate displayed in (a) increases very sharply within a few hundreds of seconds. Details of the time evolution are given in (b) where the total x-axis corresponds to 864 s. The radon originated in the porous medium reaches a maximum at t=191 s while the radon originated in the cavity starts reaching the ground surface only after 191 s. After a few days, the flow rate of radon scavenged from the porous medium is still increasing; this is probably due to the fact that the pressure progressively increases around the fractures and this induces a larger contribution of the porous medium. During the same time, the flow rate of radon contributed from the cavity decreases, and the overall radon flow rate as well.

The volumetric activity concentrations of radon expected at the monitoring site following emission at the test site is displayed in Fig.7c. It is derived from the surface flow rate shown in Fig.7a. No ^{222}Rn atmospheric background is considered here. The dilution factor η and the delay of 1 day between the two sites are taken into account, as well as the corresponding radioactive decay with time. Moreover, measurements are integrated over

6-hours intervals. Therefore, the small-scale variations of the radon flow rate shown in (b) for the first moments are smoothed out. Generally speaking, the radon originated in the porous medium is significantly larger than the radon from the cavity, at least for the first 10 days. Then, the two contributions are roughly of the same order of magnitude.

A reasonable order of magnitude of the background value of ^{222}Rn being 50 Bq/m^3 (Richon et al., 2005), it is hopeless to detect such minute additions of radon in the atmosphere at the monitoring site. Even if we had considered a dilution factor $\eta = 10^{-14}$ s m^{-3}, which represents the most favorable case, the contribution of ^{222}Rn from the test site following an UNE would remained undetected at the monitoring site.

B. ^{133}Xe

For its own sake as for comparison with the tracers studied in the previous sections, let us now investigate the mass flow rates at the test site and the activity concentrations at the monitoring site of radioxenon, a major trigger to detect and discriminate UNEs (e.g., Kalinowski et al., 2010). While 4 radioactive xenon isotopes are of interest, all together referred to as radioxenon, we focus here on ^{133}Xe, the major one. The other isotopes could be computed in the same way. Radioxenon is created in the nuclear cavity by fission of uranium or plutonium. The physical constants of ^{133}Xe are an atomic mass M_{Xe} of 0.133 kg/mol, a molecular diffusion coefficient D= 1.25 10^{-6} m^{2}s^{-1} and a radioactive decay constant λ_{Xe} = 1.528 10^{-6} s^{-1}. For a 150 kt-explosion, the quantity initially produced in the cavity is ca. 1.5 mole (e.g., Sun et al., 2014), i.e. 0.2 kg. Again the initial mass fraction of ^{133}Xe in the damaged zone depends on the initial pressure P_0. Calculations were performed for the three values of the initial cavity pressure P_0= 50, 100 and 200 bars. The porosity of the matrix is $\epsilon = 0.05$ and the number of fractures is $N_f = 192$.

Results are shown in Fig.8. At the test site, the ^{133}Xe flow rate reaches a maximum in very short times (Fig.8a) of the order of a few hundred seconds, as for water (Fig.3a-c) and radon (Fig.7b) also contributed, at least in part, by the nuclear cavity and in contrast with CO_2 (Fig.6a), which is contributed by the soil. Then, the activity decreases more or less exponentially.

Fig.8b shows the ^{133}Xe activity concentrations expected at the monitoring site. Here again, it is derived from the surface flow rate, as shown in Fig.8a. No ^{133}Xe atmospheric

background is considered here, which is known to be highly variable (Achim et al., 2016). The dilution factor η and the delay of 1 day between the two sites are taken into account, as well as the corresponding radioactive decay with time. Moreover, measurements are integrated over 6-hours intervals, mimicking a sampling and analysis system. The ^{133}Xe activity decreases exponentially, but during 7 to 14 observation days at the monitoring site, they are above the minimum detection concentration of the most recent radioxenon analytical system (see Topin et al. 2020, Brander et al. 2022, Aldener et al. 2023). Therefore, radioxenon originating from the nuclear test site should be detected at the monitoring site during 1 week to 2 weeks (depending on the initial pressure in the cavity), providing no stronger ^{133}Xe background signal is superimposed.

VI. CONCLUDING REMARKS

Our work highlights the importance of focusing attention not only on the monitoring stations, but also on the nuclear test site. This study shows that it should be feasible to enhance detection of radioxenon related to an underground nuclear explosion at a given monitorig station by detecting, a short time beforehand at the test site, the concomitant emission of water vapor by satellite imaging. In addition to backward atmospheric transport modeling inherently subjected to multiple Possible Source Regions (e.g., Ringbom et al., 2014) and radioxenon background, this new technique would bring direct evidence that gas is emitted to the atmosphere from the test site. Although depending on the natural content of the atmosphere in water vapor, this technique could be applied across all continents except in the tropical zone where the large water vapor content in the atmosphere might prevent detection of small UNEs-related emissions. Additionnal remote sensing operated before the event and atmospheric modeling could be used to give a reliable background water vapor content, from which the UNEs-related emissions could be more easily detected.

Although commonly detected in other applications where plumes are much bigger, CO_2 contributed from the soil then scavenged by the gas emitted following an UNE is not likely to be detected from satellite imaging. In some particular geological settings, an additional contribution of CO_2 from the nuclear cavity might provide an enhanced contribution potentially detectable. A yet unexplained distinctive circular shape at the ground surface was observed in our simulations. If confirmed as a general feature, this distinctive characteristic

could also be a detection means. Although it is contributed from the entire rock body up to the ground surface, including from vaporization of the cavity material, ^{222}Rn cannot be detected neither at the monitoring site, where the dilution and the background level are high, nor at the nuclear test site where no remote sensing technique is able to image its emission.

Thanks to this first appraisal of the detectability of tracer gas emissions at the ground surface of a nuclear test site following an UNE, a more rigourous modeling of the signal expected on various satellite probes can now be undertaken using inversion methods as well as the satellite characteristics.

Acknowledgments: The authors thank Pascal Achim for providing helpful discussions during the development of this work. We also thank Sylvia Generoso for sharing simulations of the dilution factor associated to atmospheric transport between the DPRK nuclear test site and the Takasaki monitoring station, and Rodolphe Marion for guiding us to the detectability of gas emissions from remote sensing techniques.

Declaration: No specific declaration

[1] Achim, P., Generoso S., Morin M., Gross P., Le Petit G., & Moulin (2016). Characterization of Xe-133 global atmospheric background: Implications for the International Monitoring System of the Comprehensive Nuclear-Test-Ban Treaty. *Journal of Geophysical Research: Atmospheres*, 121(9): 4951-4966.

[2] Adler, P.M. (1992). *Porous media: geometry and transports.* Butterworth/Heinemann.

[3] Adler, P.M., Thovert, J.-F., & Mourzenko, V.V. (2012). *Fractured porous media.* Oxford University Press.

[4] Aldener, M., Axelsson, A., Fritioff, T., Kastlander, J., Ringbom, A. (2023). SAUNA III - The next generation noble gas system for verification of nuclear explosions. *Journal of Environmental Radioactivity*, 262: 107159.

[5] Barenblatt, G.I., Zheltov, Iu.P., & Kochina, I.N. (1960). Basic concepts in the theory of seepage of homogeneous liquids in fissured rocks, *Soviet Appl. Math. Mech. (P.M.M.), 24*, 852–864.

[6] Boardman, C.C., Rabb, D.D., & McArthur, R.D. (1964). Responses of Four Rock Mediums to Contained Nuclear Explosions. *Journal of Geophysical Research, 69* 3457–3469.

[7] Bogdanov, I.I., Mourzenko, V.V., Thovert J.-F., & P.M. Adler (2003). Effective permeability of fractured porous media in steady-state flow, *Water Resources Research*, 39, 10.1029/2001WR000756.

[8] Bourret, S.M., Kwicklis, E.M., Miller, T.A., & Stauffer, P.H. (2018). Evaluating the importance of barometric pumping for subsurface gas transport near an underground nuclear test site. *Vadose Zone Journal*, DOI: 10.2136/vzj2018.07.0134.

[9] Bourret, S.M., Kwicklis, E.M., Harp, D.R., Ortiz, J.P., & Stauffer, P.H. (2020). Beyond Barnwell: Applying lessons learned from the Barnwell site to other historic underground nuclear tests at Pahute Mesa to understand radioactive gas-seepage observations. *Journal of Environmental Radioactivity 222*, 106297.

[10] Bovensmann, H., Buchwitz M., Burrows J. P., Reuter M., Krings T., Gerilowski, K., Schneising, O., Heymann, J., Tretner, A., & Erzinger J. (2010). A remote sensing technique for global monitoring of power plant CO_2 emissions from space and related applications. *Atmos. Meas. Tech.*, 3(4): 781-811.

[11] Brander, S., Baur, S., Krais, R., Ross, J. O., Orr, A., Sayne, R., Howard, M., Mayer, M.l., Panisko, M., Hayes, J. C., Bollhöfer, A. (2022). Phase II testing of Xenon International on Mount Schauinsland, Germany. *Journal of Environmental Radioactivity*, 255: 107034.

[12] Burnett, J.L., Stewart, T.L., Keillor, M.E., & Ely, J.H. (2021). Investigating the detection of underground nuclear explosions by radon displacement. *Journal of Environmental Radioactivity*, 229-230: 106541.

[13] Carothers, J.E. , Brownlee, R., Campbell, B., Johnson, G., & Ross, B. (1995). Caging the dragon-The containment of underground nuclear explosions, U.S. Department of Energy, Report DOE/NV-388, 726 p.

[14] Carrigan, C. R., Heinle, R. A., Hudson, G. B., Nitao, J. J. & Zucca, J. J. (1996). *Trace gas emissions on geological faults as indicators of underground nuclear testing*, *Nature*, **382**, p. 528-531.

[15] Carrigan, C.R., Sun, Y., Hunter, S.L., Ruddle, D.G, Wagoner, J.L., Myers, K.B.L., Emer, D.F., Drellack, S.L., & Chipman, V.D. (2016). Delayed signatures of underground nuclear explosions. *Scientific Reports*, 6: 23032.

[16] Carrigan C.R., Sun, Y.W., & Simpson M.D. (2019). The characteristic release of noble gases from an underground nuclear explosion. *J. Environ.Radioact.* 196, 91-97.

[17] Carrigan, C.R., Sun, Y.W., Hunter, S.L., Ruddle, D.G., Simpson, M.D., Obi, C.M., Huckins-Gang, H.E., Prothro, L.B., & Townsend, M.J. (2020). Gas transport across the low-permeability containment zone of an underground nuclear explosion. *Sci. Rep.* 10, 1437. https://doi.org/10.1038/s41598-020-58445-1.

[18] Carrigan, C.R., Sun, Y., & Antoun, T. (2022). Evaluation of subsurface transport processes of delayed gas signatures applicable to underground nuclear explosions. *Scientific Reports*, 12(1): 13169.

[19] Coblentz, D., Pabian, F. (2015). Revised Geologic Site Characterization of the North Korean Test Site at Punggye-ri *Science & Global Security*, 23(2): 101-120.

[20] Derlich, S. (1970). Underground nuclear explosion effects in granite rock fracturing, *Symposium on Engineering with Nuclear Explosive*, Las Vegas, Nevada, pp. 505–518.

[21] Eslinger, P.W., Bowyer, T.W., Cameron, I.M., Hayes, J.C., & Miley, H.S. (2015). Atmospheric plume progression as a function of time and distance from the release point for radioactive isotopes. *Journal of Environmental Radioactivity*, 148: 123-129.

[22] Gao, B.-C., Kaufman, Y.J. (2003). Water vapor retrievals using Moderate Resolution Imaging Spectroradiometer (MODIS) near-infrared channels. *Journal of Geophysical Research: Atmospheres*, 108(D13).

[23] Goodwin, M.A., Britton, R., & Davies, A.V., (2021). A Consideration of Radioxenon Detections Around the Korean Peninsula. *Pure and Applied Geophysics*, 178(7): 2651-2664.

[24] Guillon, S. (2013) Detection and migration of gas in geological media: Experiments and modeling at the Roselend Natural Laboratory (in French). Ph.D. thesis, Institut de Physique du Globe, Paris, France, p. 270.

[25] Harp, D.R., Ortiz, J.P., Pandey, S., Karra, S.,·Anderson, D., Bradley, C., Viswanathan, H., & Stauffer, P.H. (2018). Immobile Pore-Water Storage Enhancement and Retardation of Gas Transport in Fractured Rock, *Transp Porous Med 124*, 369—394, /doi.org/10.1007/s11242-018-1072–8.

[26] Harp, D.R., Ortiz, J.P., & Stauffer, P.H. (2019). Identification of dominant gas transport frequencies during barometric pumping of fractured rock. *Scientific Reports 9*, 9537.

[27] Harp, D.R., Bourret, S.M., Stauffer, P.H., & Kwicklis, E.M. (2020). Discriminating Underground Nuclear Explosions Leading To Late-Time Radionuclide Gas Seeps. *Geophysical Research Letters 47*, e2019GL086654.

[28] Harten A. (1993). High Resolution Schemes for Hyperbolic Conservation Laws. *Journal of Computational Physics*, **49**, 357.

[29] He, J., Liu, Z. (2021). Refining MODIS NIR Atmospheric Water Vapor Retrieval Algorithm Using GPS-Derived Water Vapor Data. *IEEE Transactions on Geoscience and Remote Sensing*, 59(5): 3682-3694.

[30] Huseby, O., Thovert, J.-F., & Adler, P.M. (1997). Geometry and topology of fracture systems, *Journal of Physics A: Mathematical and Theoretical*, **30**, 1415-1444.

[31] Johnson, G.W., Higgins, G.H., & Violet, C.E. (1959). Underground nuclear detonations. *Journal of Geophysical Research 64*, 1457–1470.

[32] Johnson, C., Aalseth, C.E., Alexander, T.R., Bowyer, T.W., Chipman, V., Day, S., Drellack, A.R., Fast, J.E., Fritz, B.G., Hayes, J.C., Huckins-Gang, H.E., Humble, P., Kirkham, R.R., Lowrey, J.D., Mace, E.K., Mayer, M.F., McIntyre, J.I., Milbrath, B.D., Panisko, M.E., Paul, M.J., Obi, C.M., Okagawa, R.K., Olsen, K.B., Ripplinger, M.D., Seifert, A., Suarez, R., Thomle, J., Townsend, M.J.,Woods, V.T. & L. Zhong (2019). Migration of noble gas tracers

at the site of an underground nuclear explosion at the Nevada National Security Site. *Journal of Environmental Radioactivity*, 208–209 106047

[33] Jordan, A.B., Stauffer, P.H., Zyvoloski, G.A., Person, M.A., MacCarthy, J.K., & Anderson, D.N. (2014). Uncertainty in Prediction of Radionuclide Gas Migration from Underground nuclear Explosions. *Vadose Zone Journal 13*, 1–13.

[34] Jordan, A.B., Stauffer, P.H., Knight, E.E., Rougier, E., & Anderson, D.N. (2015). Radionuclide Gas Transport through nuclear Explosion-Generated Fracture Networks. *Scientific Reports 5*, 18383.

[35] Kalinowski, & M., Schulze, J. (2002). Radionuclide monitoring for the Comprehensive Nuclear Test Ban Treaty. *Journal of Nuclear Materials Management*, 30: 57-67.

[36] Kalinowski, M.B. et al. (2010). Discrimination of Nuclear Explosions against Civilian Sources Based on Atmospheric Xenon Isotopic Activity Ratios. *Pure and Applied Geophysics*, 167(4-5): 517-539.

[37] Koudina, N., Gonzalez, G.R., Thovert, J.-F.& Adler P.M. (1998). Permeability of three-dimensional fracture networks, *Physical Review E.*, **57**, 4466-4479,.

[38] Lowrey, J.D., Biegalski, S.R., Osborne, A.G., & Deinert, M.R. (2013). Subsurface mass transport affects the radioxenon signatures that are used to identify clandestine nuclear tests. *Geophysical Research Letters 40*, 111–115.

[39] Lowrey, J.D., Biegalski, S.R., & Deinert, M.R. (2013). UTEX modeling of radioxenon isotopic fractionation resulting from subsurface transport. *Journal of Radioanalytical and Nuclear Chemistry*, 296(1): 129-134.

[40] Lowrey, J.D., Osborne, A.G., Biegalski, S.R., & Deinert, M.R. (2015). Comparison of Numerically Stable Methods for Implementation of a Double Porosity Model with First-Order Reaction Terms. *Transport in Porous Media*, 106: 33-45.

[41] Mao, K. B., Li, H. T., Hu, D. Y., Wang, J., Huang, J. X., Li, Z. L., Zhou, Q. B., Tang, H. J. (2010). Estimation of water vapor content in near-infrared bands around 1 μm from MODIS data by using RM–NN. *Optics Express*, 18(9): 9542-9554.

[42] Maurer, C., Baré, J., Kusmierczyk-Michulec, J., Crawford, A., Eslinger, P. W., Seibert, P., Orr, B., Philipp, A., Ross, O., Generoso, S., Achim, P., Schoeppner, M., Malo, A., Ringbom, A., Saunier, O., Quèlo, D., Mathieu, A., Kijima, Y., Stein, A.l., Chai, T., Ngan, F., Leadbetter, S. J., De Meutter, P., Delcloo, A., Britton, R., Davies, A., Glascoe, L. G., Lucas, D. D.,

Simpson, M. D., Vogt, P., Kalinowski, M., Bowyer, T. W. (2018). International challenge to model the long-range transport of radioxenon released from medical isotope production to six Comprehensive Nuclear-Test-Ban Treaty monitoring stations. *Journal of Environmental Radioactivity*, 192: 667-686.

[43] McClatchey, R.A., Fenn, R.W., Selby, J.E.A., Volz, F.E., & Garing, J.S. (1972). Optical properties of the atmosphere, 3rd ed, Air Force Cambridge Research Laboratories, Hanscom Field, Bedford, Massachusetts, 114 pp.

[44] Nield, D.A., & Bejan, & A. (2006). Convection in porous media, 3rd edition, Springer, Berlin.

[45] Nilson, R. H., E. W. Peterson, K. H. Lie, N. R. Burkhard, & J. R. Hearst (1991). Atmospheric pumping: A mechanism causing vertical transport of contaminated gases through fractured permeable media, *J. Geophys. Res., 96*, 21,933-–21,948.

[46] Olsen, K.B. et al. (2016). Noble gas migration experiment to support the detection of underground nuclear explosions. *Journal of Radioanalytical and Nuclear Chemistry*, 307(3): 2603-2610.

[47] Pazdniakou, A., Mourzenko, V.V., Thovert, J.-F., Adler, P.M., & Pili, E. (2022). Two-phase flow, heat and mass transfer and tracer transport to the atmosphere from underground nuclear cavities through fractured porous media *Pure Appl. Geophys.*, doi.org/10.1007/s00024-022-03038-4.

[48] Pellegrini, M., Aghakhani, A., Guzzini, A., Saccani, C. (2022). Modification of Fraser′s Method for the Atmospheric CO_2 Mass Estimation by Using Satellite Data. *Atmosphere*, 13(6): 866.

[49] Richon, P., Perrier, F., Sabroux, J.C., Trique, M., Ferry, C., Voisin, V., & Pili, E. (2005) Spatial and time variations of radon-222 concentration in the atmospheres of a dead-end horizontal tunnel. *Journal of Environmental Radioactivity*, 78, 179-198.

[50] Ringbom, A., Axelsson, A., Aldener, M., Auer, M., Bowyer, T. W., Fritioff, T., Hoffman, I., Khrustalev, K., Nikkinen, M., Popov, V., Popov, Y., Ungar, K., Wotawa, G. (2014) Radioxenon detections in the CTBT international monitoring system likely related to the announced nuclear test in North Korea on February 12, 2013. *Journal of Environmental Radioactivity*, 128: 47-63.

[51] Risk, D., Kellman, L., & Beltrami, H. (2002). Carbon dioxide in soil profiles: Production and temperature dependence GEOPHYSICAL RESEARCH LETTERS, VOL. 29, 1087, 10.1029/2001GL014002.

[52] Schlaepfer, D. (1998). Differential Absorption Methodology for Imaging Spectroscopy of Atmospheric Water Vapor. *Ph. D. Thesis*, University of Zürich, Switzerland, 131 pp.

[53] Stohl, A., Hittenberger, M., Wotawa, G. (1998). Validation of the lagrangian particle dispersion model FLEXPART against large-scale tracer experiment data. *Atmospheric Environment*, 32(24): 4245-4264.

[54] Sun, Y., & Carrigan, C. (2012). Modeling Noble Gas Transport and Detection for the Comprehensive Nuclear-Test-Ban Treaty. *Pure and Applied Geophysics*, 171, 735–750.

[55] Sun, Y., Carrigan, C., & Hao, Y. (2014). Radioxenon production and transport from an underground nuclear detonation to ground surface. *Pure and Applied Geophysics*, 172, 243–265.

[56] Sun Y., & Carrigan, C.R. (2016). Thermally driven advection for radioxenon transport from an underground nuclear explosion. *Geophysical Research Letters 43(9),4418–4425*, 10.1002/2016GL068290.

[57] Sun, Y., Carrigan, C.R., Pili, E., & Antoun, T. (2022). Implications of Underground Nuclear Explosion Cavity Evolution for Radioxenon Isotopic Composition. *Pure and Applied Geophysics*, 10.1007/s00024-022-03026-8.

[58] Sweby, P.K. (1984). High resolution schemes using flux limiters for hyperbolic conservation laws. *SIAM Journal on Numerical Analysis*, **21**, 995-1011.

[59] Topin, S., Gross, P., Achim, P., Generoso, S., Cagniant, A., Delaune, O., Morin, M., Philippe, T., Fontaine, J.-P., Moulin, C., Douysset, G., Le Petit, G. (2020). 6 months of radioxenon detection in western Europe with the SPALAX-New generation system - Part1: Metrological capabilities. *Journal of Environmental Radioactivity*, 225: 106442.

[60] Varon, D.J., Jacob, D.J., McKeever, J., Jervis, D., Durak, B.O.A., Yan Xia, & Yi Huang et al. (2018). Quantifying methane point sources from fine-scale satellite observations of atmospheric methane plumes. *Atmos. Meas. Tech.*, 11(10): 5673-5686.

[61] Wollenberg, H., Straume, T., Smith, A., & King, C.Y. (1977). Variation in radon-222 in soil and groundwater at the Nevada Test Site, *LBNL report LBL-5905*, 10 p.

[62] Wulfmeyer, V., Hardesty, R. M., Turner, D. D., Behrendt, A., Cadeddu, M. P., Di Girolamo, P., Schlüssel, P., Van Baelen, J., Zus, F. (2015). A review of the remote sensing of lower tropospheric thermodynamic profiles and its indispensable role for the understanding and the simulation of water and energy cycles. *Reviews of Geophysics*, 53(3): 819-895.

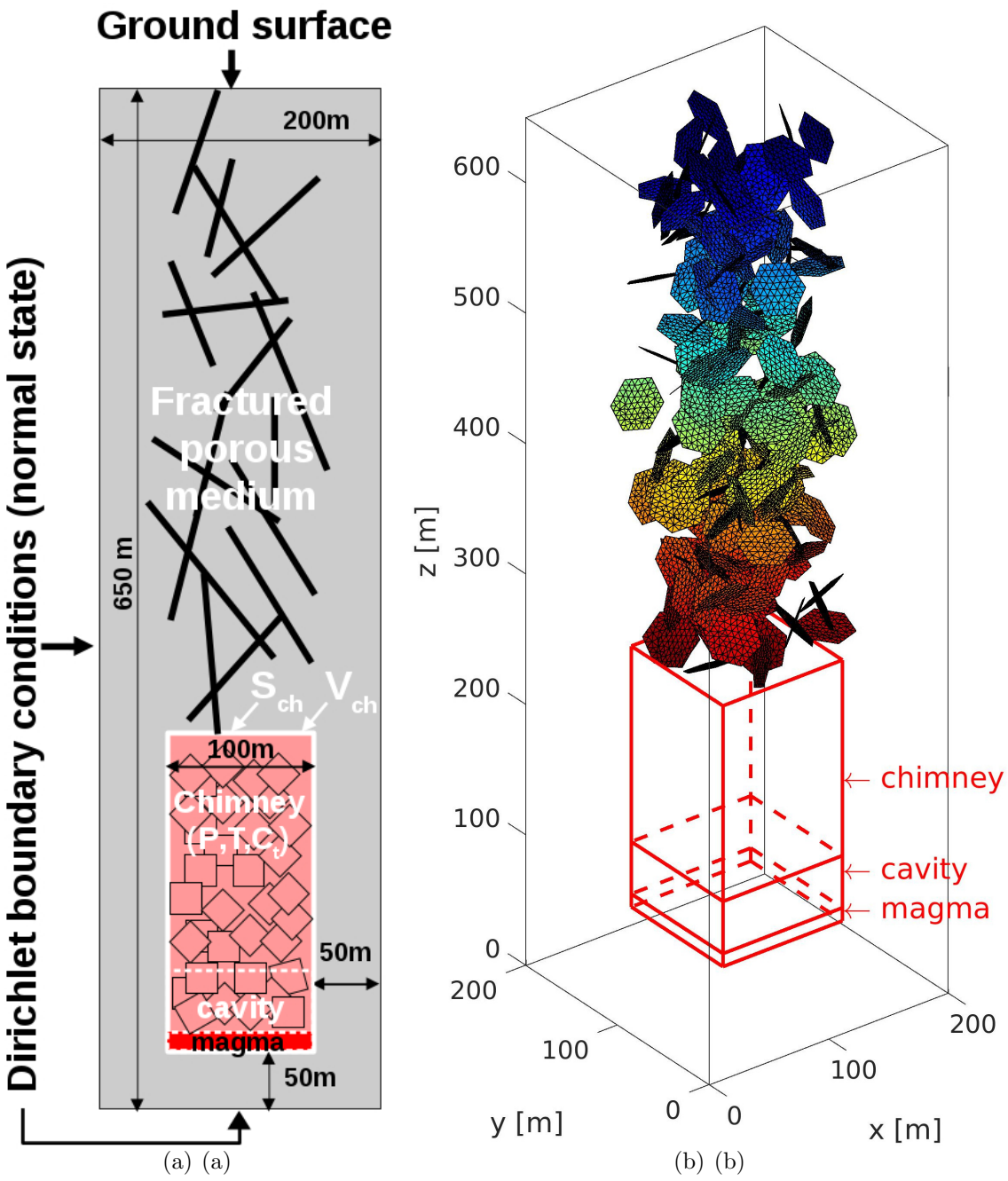

FIG. 1. The complete geometry of the model, taken from Pazdniakou et al. (2022). (a) Schematized vertical mid-cross section of the simulation domain. (b) The percolating fracture network of 192 individual hexagonal fractures meshed with triangles inside the simulation domain. The red lines and zones indicate the location of the damaged zone, consisting of the chimney, the cavity and the magma.

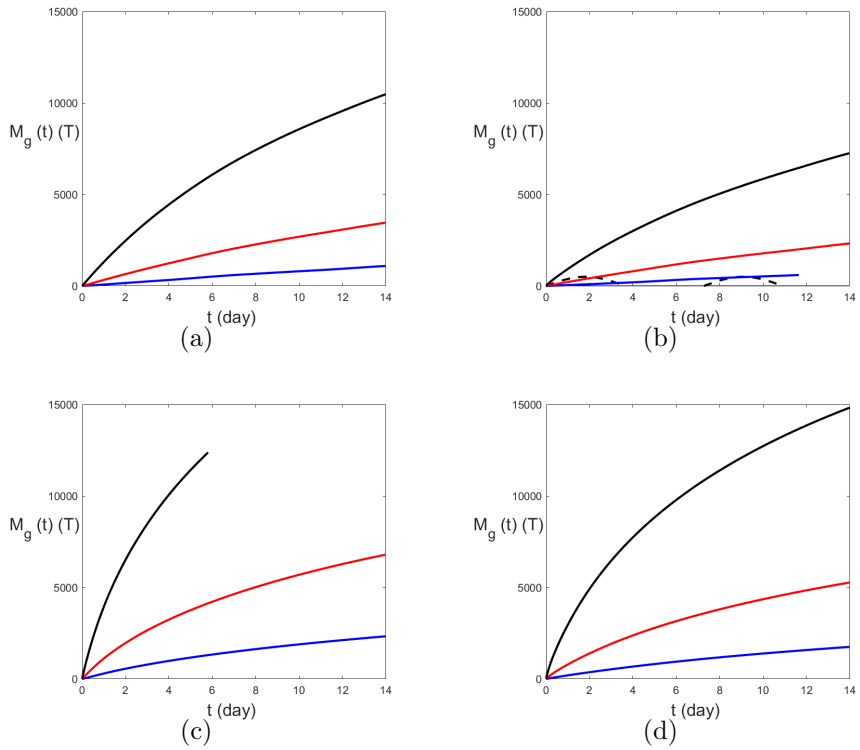

FIG. 2. The total mass of air $M_g(t)$ (tons) transferred to the atmosphere as a function of time t (day) for the three initial pressures in the cavity P_0 and for various petrophysical parameters of the fractured porous medium outside of the damaged zone. Data are for: first line N_f=192, second line N_f=384; left row ϵ=0.01, right row ϵ=0.05. The broken curve at the bottom of (b) provides the positive fluctuations of the atmospheric pressure $p(z = 650)$ (1) with an arbitrary vertical scale. Initial cavity pressure: P_0=50 (blue), 100 (red), 200 (black) bars.

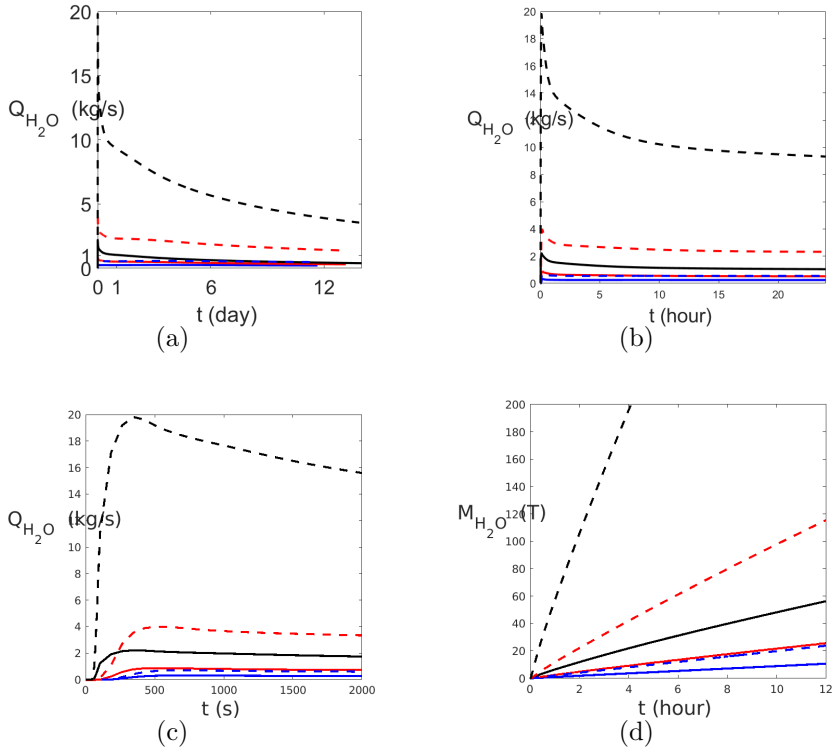

FIG. 3. The water vapor contained in the cavity transferred to the atmosphere for the three initial pressures in the cavity (for color convention in all the subfigures see Fig.2). The solid and broken lines correspond to a mass fraction in the cavity+chimney equal to $22.3/P_0$ and 1, respectively. Petrophysical parameters: $\epsilon = 0.05$, $N_f = 192$. (a), (b) and (c) The mass flow rate Q_{H_20} (kg/s) as a function of time t for the first 14 days, the first 24 hours and the first 2000 seconds, respectively. (d) The total mass of water M_{H_20} (ton) transferred to the atmosphere as a function of time t (hour) for the 12 first hours.

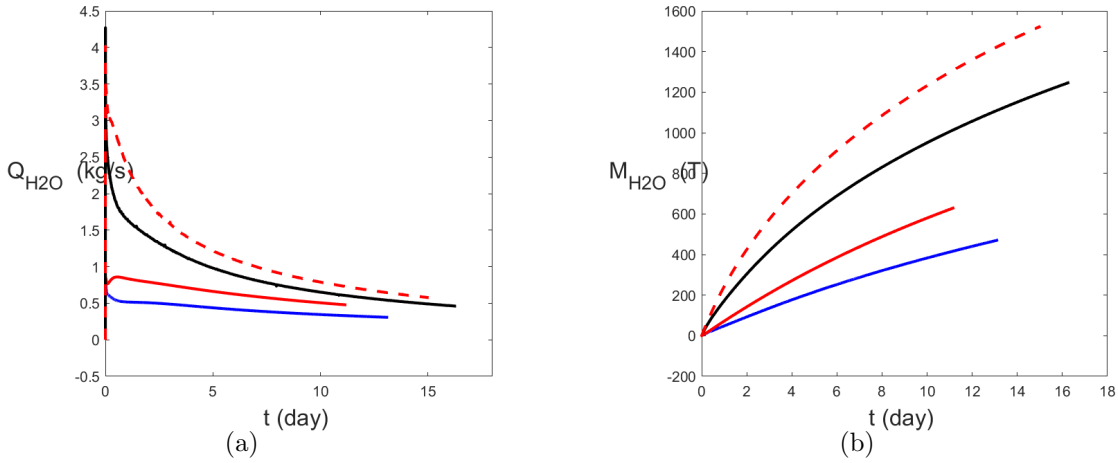

FIG. 4. Influence of the petrophysical properties of the surrounding medium on the water mass flow rate and on the total water mass transferred to the atmosphere for P_0=100 bars. (a) The mass flow rate Q_{H_20} (kg/s) as a function of time t (day). (b) The total mass of water M_{H_20} (ton) transferred to the atmosphere as a function of time t (day). Color convention: blue (ϵ=0.05, N_f=192), red (ϵ=0.01, N_f=192), black (ϵ=0.05, N_f=384), broken red (ϵ=0.01, N_f=384).

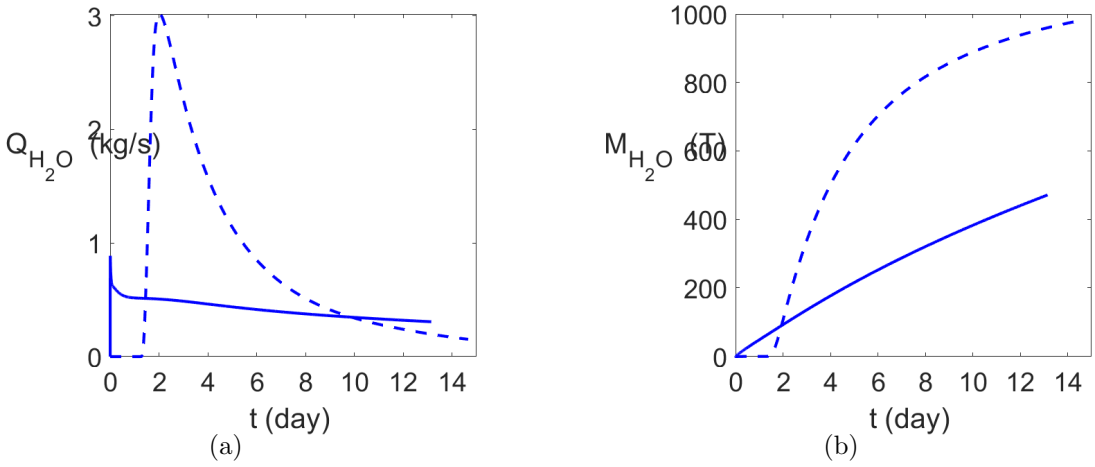

FIG. 5. Comparison between the fractured porous medium model (solid line) and the homogeneous one (broken line): P_0=100 bars, ϵ=0.05, N_f=192. (a) The mass flow rate Q_{H_20} (kg/s) as a function of time t (day). (b) The total mass of water M_{H_20} (ton) transferred to the atmosphere as a function of time t (day).

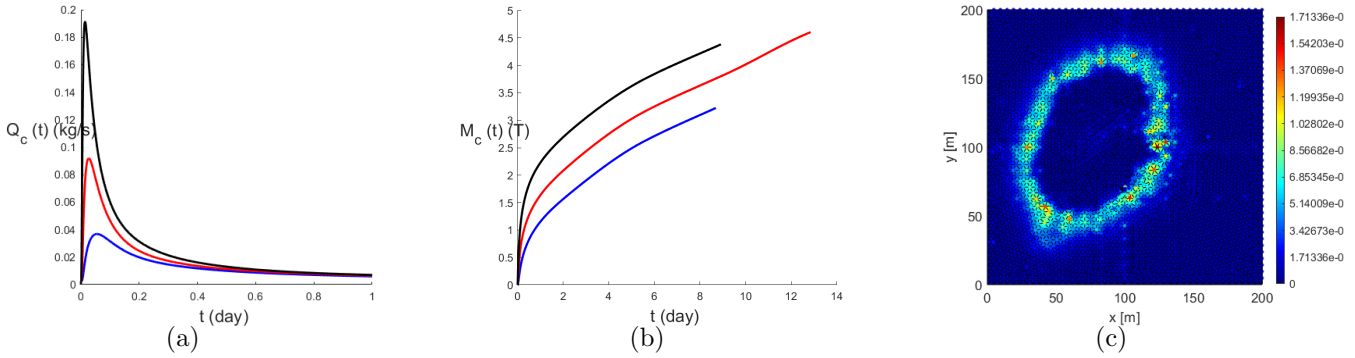

FIG. 6. CO_2 emission at the nuclear test site. Petrophysical conditions: ϵ=0.01, N_f=192 for the rock body, ϵ=0.3 and no fractures in the ca. 6-m thick soil layer on the top of it. Initial cavity pressure: P_0=50 (blue), 100 (red), 200 (black) bars. (a) Mass flow rate as a function of time, showing that air flow following the UNE wipes out the carbon dioxide present in the soil before reaching a stationary regime. (b) CO_2 mass transferred to the atmosphere. (c) Planar view of the mass flow rate of CO_2 at the ground surface at t=12.9 days, showing a distinctive circular shape.

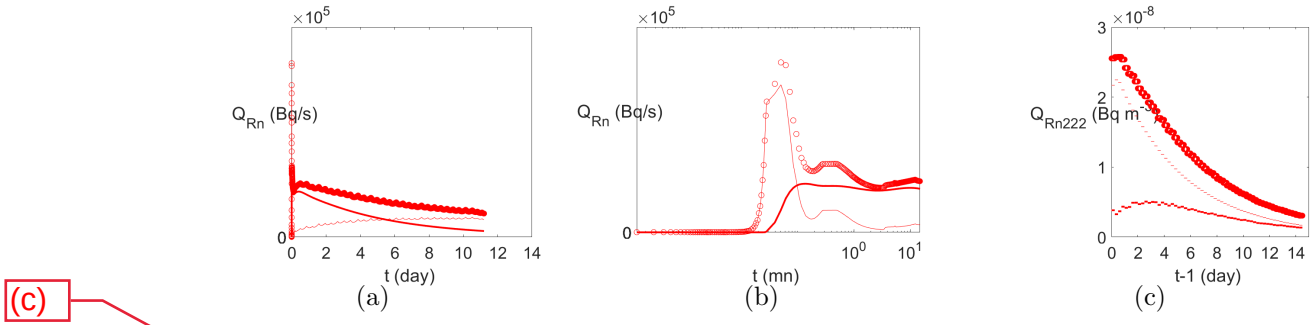

FIG. 7. Radon emission at the nuclear test site (a) and (b), and activity concentration at the monitoring site (b) as function of time. Petrophysical conditions: ϵ=0.01, N_f=192. Initial cavity pressure: P_0=100 bars. Line convention: radon originated in the porous medium (thin line), radon originated in the cavity (medium line), sum (thick line or dots). The x-axis labelled (t-1) in days takes into account an atmospheric transport delay of 1 day.

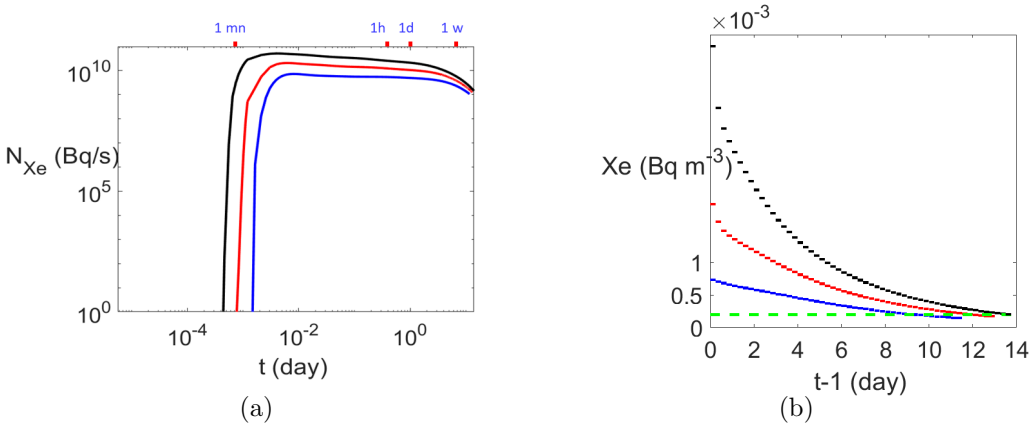

FIG. 8. Flow rate of xenon-133 emitted at the nuclear test site (a) and activity concentration at the monitoring site (b) as functions of time. Petrophysical conditions: ϵ=0.05, N_f=192. Initial cavity pressure: P_0=50 (blue), 100 (red), 200 (black) bars. In (b), the horizontal broken line corresponds to the detection limit and the x-axis labelled (t-1) in days takes into account an atmospheric transport delay of 1 day.

Appendix A: Gaussian plume inversion method

The Gaussian plume inversion method described below is derived from Bovensmann et al. (2010) and Varon et al. (2018). The mass flow rate at the test site Q (in kg/s) contributes to an excess $\Delta\Omega(x,y)$ (in kg/m^2) of water vapor at a point of coordinates (x, y) according to

$$Q = U\Delta\Omega(x,y)(\sqrt{2\Pi}\sigma_y(x)e^{\frac{y^2}{2\sigma_y(x)^2}}) \tag{A1}$$

where U is the wind along the x-axis (in m/s), $\sigma_y(x)$ the horizontal dispersion along the y-axis (in m). Classically, one takes

$$\sigma_y(x) = a(\frac{x}{x_0})^{0.894} \tag{A2}$$

where x_0= 1000 m and a characterizes the stability of the atmosphere (Pasquill stability classes). For the common stability class C, a= 104.

Setting the value of y to 0 restricts the calculation on the x-axis. Hence, (A1) and (A2) imply

$$Q = U\Delta\Omega(x,0)\sqrt{2\Pi}(\frac{x}{1000})^{0.894} \tag{A3}$$

Then, we set values for x to 10 and 100 m and values for U to 0.1, 1 and 10 m/s in (A3) and compute the corresponding values of Q, for a range of detectable excess water vapor corresponding to the various climate zones and seasons as given in Table I. These values of Q are then compared to the values of the mass flow rates of water vapor emitted at the nuclear test site following an UNE and computed for various conditions as given in Table II. When the computed values of Q match the mass flow rates of water vapor potentially emitted at the nuclear test site, a detection is possible.

TABLE I. Integrated water vapor content in the atmosphere for various climate zones and seasons (from McClatchey et al., 1972; Schlapfer, 1998) and detectable 2% variation of this quantity.

Climate zones and seasons	**Water vapor** (kg/m^2)	**Detectable variation (2%)** (kg/m^2)
Tropical	41.98	0.84
Midlatitude Summer	29.82	0.60
Subartic Summer	21.20	0.42
Midlatitude Winter	8.67	0.17
Subartic Winter	4.23	0.08

TABLE II. Mass flow rates of water vapor emitted to the atmosphere following an UNE for the low and high water contents and for the 3 initial cavity pressure values. The symbols *, **, ***, **** and ***** stand for 5 classes of mass flow rates to be compared with those calculated for detectability with various meteorological conditions (see Tables III and IV).

Initial cavity pressure	**Mass flow rates (low)**	**Mass flow rates (high)**
bar	kg/s	kg/s
50	0.25*	0.75**
100	0.75**	4****
200	1.75***	17.5*****

TABLE III. Mass flow rates of water vapor obtained from (A3) and necessary to be emitted to the atmosphere for detection (2% variation of the water content). * means detection and refers to Table II.

Climate zones	**Distance along x-axis**	**Wind speed: 0.1**	**Wind speed: 1**	**Wind speed: 10**
	m	m/s	m/s	m/s
Tropical	10	0.36**	3.6	36
-	100	2.8****	28	279
Midlatitude Summer	10	0.25*	2.5****	25
-	100	2****	20	198
Subartic Summer	10	0.18*	1.8***	18****
-	100	1.4***	14****	141
Midlatitude Winter	10	0.07*	0.74**	7.4****
-	100	0.58**	5.8****	58
Subartic Winter	10	0.04*	0.36**	3.6***
-	100	0.28*	2.8***	28

TABLE IV. Mass flow rates of water vapor obtained from (A3) and necessary to be emitted to the atmosphere for detection (5% variation of the water content). * means detection and refers to Table II.

Climate zones	**Distance along x-axis**	**Wind speed: 0.1**	**Wind speed: 1**	**Wind speed: 10**
	m	m/s	m/s	m/s
Tropical	10	0.89	8.92*****	89.2
-	100	6.98*****	69.8	698
Midlatitude Summer	10	0.63**	6.33*****	63.3
-	100	5.0*****	49.6	496
Subartic Summer	10	0.45**	4.50*****	45.0
-	100	3.5****	3.53	353
Midlatitude Winter	10	0.18*	1.84****	18.4
-	100	1.44***	14.4*****	144
Subartic Winter	10	0.09*	0.90***	8.98*****
-	100	0.70**	7.04*****	70.4